

# The impact of cosmic variance on simulating weak lensing surveys

Arun Kannawadi<sup>1\*</sup>, Rachel Mandelbaum<sup>1</sup>, Claire Lackner<sup>2</sup>,

<sup>1</sup>*McWilliams Center for Cosmology, Carnegie Mellon University, Pittsburgh, PA 15217, USA*

<sup>2</sup>*Kavli Institute for the Physics and Mathematics of the Universe (WPI), Todai Institutes for Advanced Study, the University of Tokyo, Kashiwa, Japan.*

30 September 2014

## ABSTRACT

According to our current understanding, galaxy shapes and morphologies should depend on various factors such as the local environment. Realistic image simulations for calibration of weak lensing analysis methods that use training samples from the Hubble Space Telescope can therefore be affected by these trends, due to the limited volume of the universe that has been surveyed by Hubble. We will show how redshift slices in a volume-limited subsample of COSMOS can be classified as overdense or underdense (or neither), and how the statistical properties of various morphological parameters such as ellipticity, Sérsic  $n$ , Bulge-to-Total ratio and color differ in these bins. This study requires a careful distinction between environment effects from large-scale structure, which we do not wish to include in simulations, and general trends in the galaxy population with redshift. We conclude with some guidance for how upcoming surveys can use COSMOS data as the basis for weak lensing simulations without having their conclusions overly affected by cosmic variance. **I have some comments on this abstract, but prefer to do all revision of the abstract at the end once the paper is finalized.**

**Key words:** Gravitational lensing: weak — Cosmology: Large-scale structure of Universe — Galaxies: evolution.

Overall comment: the figures need a *lot* of work. First, they should be in the same order as they are referenced in the text. Second, they need to be sensibly referenced in the text; you can't say "as we see..." without having a clear statement that we should be looking at Fig. 4 (or whatever). In all cases, the font size is way too small, so you should enlarge it. The rule of thumb for MNRAS and other journals is that the font size in the figures should appear the same size as the font in the text of the paper. (This is true for axis labels, tick labels, and text in the legend.) You also need to write good captions, because some people will not really read the paper, just the captions. MNRAS does not use the subfigure environment, so you should remove it. Just have the figures on top of or next to each other, and then in the caption refer to "Top panel" and "Bottom panel" or whatever. **Results have too many figures and they overlap with the bibliography. I think we should put some of the figures explicitly after the references? No, just move the figures a bit earlier in the text. It's okay for them to show up slightly before you actually discuss them. The references really should be last.**

## 1 INTRODUCTION

Major surveys such as the Hyper Suprime-Cam (HSC; Miyazaki et al. 2006), Dark Energy Survey (DES; The Dark Energy Survey Collaboration 2005), the Kiilo-Degree Survey (KIDS; de Jong et al. 2013), the Panoramic Survey Telescope and Rapid Response System (PanSTARRS; Kaiser et al. 2010), the Large Synoptic Survey Telescope (LSST; LSST Science Collaboration et al. 2009), Euclid<sup>1</sup> (Laureijs et al. 2011), Wide-Field Infrared Survey Telescope (WFIRST; Green et al. 2012) are planned to be carried out over the next decade or two that will gather huge amounts of weak lensing data that can be used to constrain cosmological parameters more precisely than ever. Weak gravitational lensing probes the nature of dark energy through both the growth of structure in the universe with redshift and the dependence of distances on the expansion rate or the Hubble parameter. However, most of the matter in the universe is made up of dark matter which cannot be detected by most of the standard astronomical/cosmological probes. Weak lensing happens

\* [akannawa@andrew.cmu.edu](mailto:akannawa@andrew.cmu.edu)

<sup>1</sup> <http://sci.esa.int/euclid/>, <http://www.euclid-ec.org>

to be the cleanest probe for this purpose. As light from the background sources passes through the foreground cluster of galaxies and dark matter profiles, the shapes get distorted. Weak lensing also causes magnification in addition to introducing a shear.

For the upcoming surveys to achieve their promise, the systematic error budget must be below the statistical error budget. This would mean that the systematic errors need to be reduced from their current typical level. One method that is commonly used to test for the presence of systematics is image simulation. Realistic simulations use samples based on images taken from the Hubble Space Telescope (HST) such as COSMOS or UDF (Ultra Deep Field), which are deep (high redshift) surveys taken over small areas of the sky. The goal of this work is to understand the systematic uncertainties that might arise due to finite size of these areas when dividing the sample into redshift slices to test for shear systematics as a function of redshift.

Previous studies have shown that any shape measurement method that uses second moments cannot be independent of the morphology and substructure of the galaxies involved. (**rephrased from GREAT3**). Hence, it is important to check any method that is proposed to measure the shape of the galaxies to check against a simulation that generates images as realistic as possible. With this in mind, the GREAT3 challenge (Mandelbaum et al. 2014) was held with the aim to test and facilitate methods for measuring weak gravitational lensing by analyzing astronomical images. Software packages like GalSim<sup>2</sup> can generate galaxy images fairly accurately, given realistic input parameters. The training dataset used in the challenge comes from the COSMOS survey, which we describe in sufficient detail in §2. While providing a good quality (high  $S/N$ ) images to be trained over, there could be some bias introduced due to the survey being a narrow one. It is known [cite refs.](#) that the shape and morphology of galaxies depend very much on their local environment. Hence, local overdensities or underdensities observed in the COSMOS' field of view (FOV) may cause the properties of the galaxies to be associated with the redshift, thus unable to distinguish between redshift evolution and large scale structure.

In this paper, we show that these large scale structure effects mentioned are indeed present in the data. The rest of the paper is structured as follows. In §3.1, we explain how we identify overdensities and underdensities, volume-limit our data in §3.2 and in §3.3, we explain how we obtain axis-ratios from the images of the galaxies. Finally, we present our results in §4 and end with conclusions in §5.

## 2 DATA

COSMOS (Scoville et al. 2007; Koekemoer et al. 2007; Leauthaud et al. 2007) is a flux-limited, narrow deep field survey covering a contiguous area of  $1.64 \text{ deg}^2$  of sky, with images taken using the Advanced Camera for Surveys (ACS) Wide Field Channel (WFC) in the Hubble Space Telescope (HST).

We apply the following set of initial cuts to the data, all of which is defined in Leauthaud et al. (2007):

(i) **MU\_CLASS=1**: Unlike SExtractor's stellar index **CLASS\_STAR** which is continuous, the **MU\_MAX** method that compares the peak surface brightness to the background level, provides a clear differentiation of galaxies (**MU\_CLASS=1**) from stars (**MU\_CLASS=2**) and other spurious objects like cosmic rays (**MU\_CLASS=3**)

(ii) **CLEAN=1**: Objects near bright stars or those containing saturated pixels were removed and the rest classify as *clean*.

(iii) **GOOD\_ZPHOT\_SOURCE =1**: This cut requires that the photometric redshifts be reliable and good enough to draw conclusions about the population. More details on what 'good' refers to can be found in Mandelbaum et al. (2011) **Need to rephrase, at least a little. I recommend being briefer and saying to see that paper for more details. Done.**

Precise shape measurements, when compared to ground-based surveys, can be made since the full width half-maximum (FWHM) of the point-spread function (PSF) is  $0.12''$ . High resolution images taken through the wide F814W filter (broad  $I$ ), after correcting for the PSF, have led to collection of postage stamp images<sup>3</sup> for the GREAT3 challenge (Mandelbaum et al. 2014), using the procedure described in Mandelbaum et al. (2011). Parametric models to most of these galaxies including Sérsic  $n$  profile fits, 2 component bulge+disk fits, axis ratios etc were done for GREAT3 challenge (Mandelbaum et al. 2014) using the method described in Lackner & Gunn (2012). This is described briefly in Sec. 3.3. In addition to the ACS/WFC (F814W) imaging, the COSMOS field has also been imaged by Subaru Suprime-Cam ( $B_j, V_j, g^+, r^+, i^+, z^+$ , NB816), the Canada-French Hawaii Telescope (CFHT;  $u^*, i^*$ ) and the KPNO/CTIO ( $K_s$ ).

Photometric redshifts were determined by Ilbert et al. (2009). The accuracy of photometric redshifts for  $m_{F814W} \leq 22.5$  is  $\sigma_{\Delta z} = 0.007(1 + z_s)$  and at fainter magnitudes, i.e.  $m_{F814W} \leq 24$ ,  $\sigma_{\Delta z} = 0.012(1 + z_s)$ . The photometric redshift values become noisy beyond  $z$  of 1 for our purposes and the various fits to the galaxies are also not very reliable beyond the apparent magnitude ( $m$ ) value of 23.5. Thus, we will exclude all galaxies that have F814W magnitude greater than 23.5. However, we will use  $m_{F814W} \leq 25.2$  sample in volume-limiting process (cf. §3.2) to calculate completeness. We take the  $z < 1.0$  flux-limited sample to fit redshift distribution models (cf. §3.1) and then restrict ourselves to  $z \leq 1$  sample for all further analysis.

Stellar mass estimates were obtained (Leauthaud et al. 2010) using the Bayesian code described in Bundy et al. (2006). Basically, a grid of models that vary in age, star formation history, dust content and metallicity are constructed to which the observed galaxy's spectral energy distribution (SED) and the photometric redshift are referenced to. At each grid point, the probability that the SED fits the model are calculated and by marginalizing over all the parameters in the grid, the stellar mass probability distribution is obtained. The median of this distribution is taken as the stellar mass estimate. A Chabrier IMF (Chabrier 2003) is assumed.

<sup>2</sup> <https://github.com/GalSim-developers/GalSim>

<sup>3</sup> <http://irsa.ipac.caltech.edu/data/COSMOS/images/galaxy-postage-stamps/>

We will analyze how the galaxy morphology and intrinsic shape depends on the environment in which they reside.

### 3 METHODS

In order to study the variation in the intrinsic ellipticity distribution and other morphological indicators with environment, there are three main steps to be carried out.

- (i) To identify overdense and underdense environments in our survey from the redshift distribution of galaxies (§3.1),
- (ii) To limit the sample such that Malmquist bias is minimized before comparing galaxies in different redshift slices (§3.2),
- (iii) To estimate the galaxy axis ratios and other morphological indicators such as Sérsic index and Bulge-to-Total ratios (§3.3).

#### 3.1 Finding overdensities

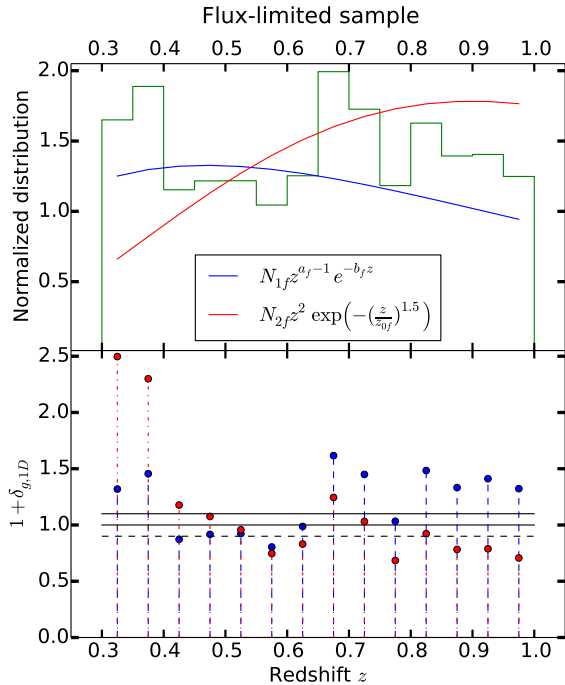


**Figure 1.** Upper panel: Redshift distribution of flux-limited ( $m_{F814W} \leq 23.5$ ) sample with bins that are 0.05 wide. Two analytical functions with best fit parameters are plotted over it. Lower panel: Plot of  $(1 + \delta_{g,1D}) = N/N_{\text{mod}}$  with each functional form as the model for each redshift bin. Give parameter values. Set minor ticks.

Weak lensing simulations will use galaxies selected in 2D redshift slices and we split our sample in a similar way to assign overdensities.

For our (flux-limited) sample of galaxies, up to  $z = 1.0$ , we fit parametric models to the histogram of photometric redshift in order to assign values of overdensity. Figures show Chi-squared distribution given by

$$p_1(z) \sim z^{a-1} \exp(-bz) \quad (1)$$

and the function given by

$$p_2(z) \sim z^2 \exp\left(-\left(\frac{z}{z_0}\right)^{1.5}\right) \quad (2)$$

that was first presented by Baugh & Efstathiou (1993) as fits to the redshift histograms. The normalization constants depend not only on the parameters but also on the lower and the upper limit of the redshifts considered. (To avoid ambiguity, you should use avoid using the same symbol in both equations. For example you could turn the  $b$ 's into  $b_1$  and  $b_2$ . Also, the normalization factors out front do not matter - they are not something that you fit for. I would say  $p(z) \propto \dots$  to avoid the need for a normalization for which you are not actually fitting.) Done. Here  $a, b$  and  $z_0$  are free parameters that are to be determined. For low  $z$ , the volume is too small to rely the overdensity values from our model fits and hence the fit is made for  $z \geq 0.3$ . Our binning width,  $\Delta z$  must be small enough so as to be able to identify localized overdensities/underdensities but large enough to not let our conclusions be affected by the errors in photometric redshift. We choose our bins to be 0.05 wide starting from  $z = 0.3$ .

Overdensity (as predicted by a given model) in a redshift bin is defined as the ratio of the difference between the value given by the histogram and the value predicted by the model to the latter:

$$\delta_{g,1D} = \frac{(N - N_{\text{mod}})}{N_{\text{mod}}} \quad (3)$$

(Call it  $\delta_{g,1D}$ , not  $\delta$ , which implies matter overdensity. Better yet would be  $\delta_{g,1D}$ , to clearly indicate this is based on a 1-dimensional slice through redshift space rather than isolating 3D overdensities.) Note that  $\delta_{g,1D}$  is model dependent. If a model and the distribution agree, then  $\delta_{g,1D} = 0$  for that model at all the redshifts.

Our decision criterion is as follows. We leave a 10% margin of safety i.e., if  $|\delta_{g,1D}| < 0.1$ , we say that the model and the actual distribution agree. We label a redshift bin overdense if at least one of the models predicts the value of  $\delta_{g,1D} > 0.1$  while the other predicts  $\delta_{g,1D} > -0.1$ , i.e., neutral or overdense and vice versa for the underdense regions. We label a redshift bin 'neutral' if both the models predicted the value of  $\delta_{g,1D}$  within the margin of safety or if one of them predicts the bin to be overdense while the other predicts it to be underdense.

We thus identify the regions  $z = 0.30 - 0.40, 0.65 - 0.75, 0.80 - 0.85$  as overdense,  $z = 0.55 - 0.65, 0.75 - 0.80$  as underdense and  $z = 0.40 - 0.55$  as unclassified.

Our classification is not very rigorous since it considers only the counts in redshift slices and compares with models that only approximately describe the redshift distribution of galaxies. Moreover, the photometric redshifts become less accurate as we go to higher redshifts (cf. §2) and no information about structure in transverse direction has been taken into account. Thus, it is important to cross-check with a more careful study of the density fields in the same field of view. Kovač et al. (2010), using a sample of  $\sim 10,000$  zCOSMOS spectra sources with  $I_{AB} < 22.5$ , have reconstructed the three dimensional overdensity field up to  $z \sim 1$ . In spite of the above mentioned shortcomings, our classification of overdensities and underdensities agrees with this work done, except for the last two high redshift bins. We believe that this disagreement is due to the errors in

our photometric redshifts and the overdensity reported in  $z = 0.875 - 1$  slice is observed by us in  $z = 0.80 - 0.85$  slice.

However, the other point to keep in mind here is that what we are doing most closely follows the way the COSMOS galaxies would be used when constructing a simulation to test weak lensing measurement methods: the sample would be divided into redshift slices using the photometric redshifts, and the shear calibration would be estimated for all galaxies in that slice. Thus, it is the apparent over- and under-densities in such a procedure that we care about here (where our main concern is testing systematics in weak lensing survey simulations, rather than learning about galaxy formation and evolution).

### 3.2 Volume limiting

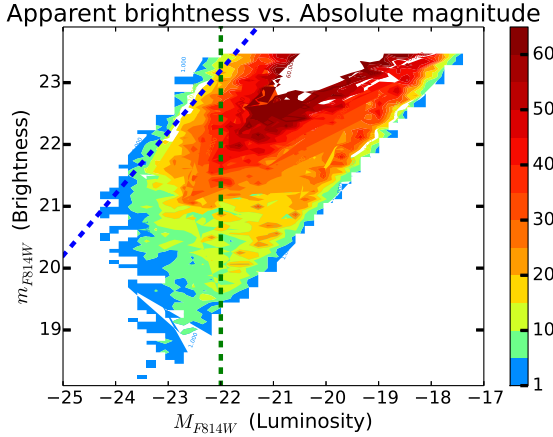


**Figure 2.** 2-D histogram of galaxies in apparent magnitude ( $m_{F814W}$ ) and absolute magnitude ( $M_{F814W}$ ) space.

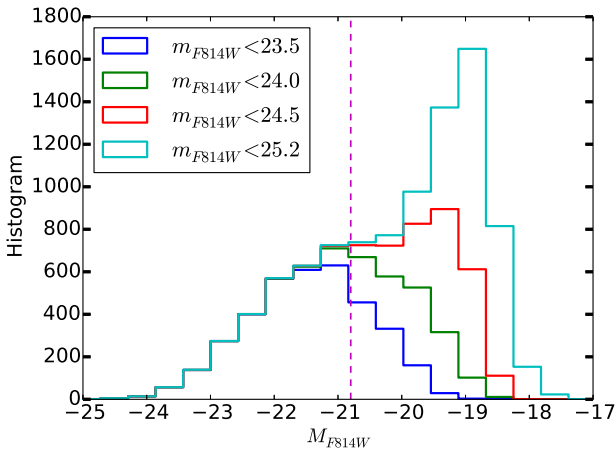


**Figure 3.** Distribution of  $M_{F814W}$  for various flux-limited samples are plotted together. The vertical line corresponds to the luminosity cut of  $-20.8$ , below which the  $m_{F814W} < 23.5$  sample has 95.3% of the galaxies in the  $m_{F814W} < 25.2$  sample.

COSMOS is a flux-limited survey and is therefore

affected by Malmquist bias, i.e. at higher redshifts, the brighter galaxies are preferentially observed. Our analysis involves comparing galaxies in different redshift slices to find significant differences in morphology, if any, so with a flux-limited sample, we would be comparing only the bright galaxies at high redshifts with bright and faint galaxies at low redshifts. For a fair comparison, we must restrict ourselves to bright galaxies at all redshifts and this is achieved by volume-limiting the sample. We generate, using the method below, a volume-limited sample that is complete upto  $z = 1$  by applying a cut on luminosity such that only galaxies intrinsically brighter than a certain threshold is considered. This threshold is set on  $K$ -corrected  $F814W$ -band magnitudes, denoted as  $M_{F814W}$ . **Is it  $i$  band, or  $I$  band? Check which one and then be self-consistent throughout the text. I think they call it  $I_{814}$ , so  $I$ . But you are still being ambiguous in sometimes calling it  $I$  and other times  $F814W$ . Pick one.** Since the parent sample contains fainter galaxies, upto  $m_{F814W} = 25.2$ , we compare the distribution of the  $m_{F814W} = 23.5$  sample with the samples containing fainter galaxies for high redshift bins, to see where the sample is no longer complete.

At  $M_{F814W} \sim -22.0$ , we see the sample is beginning to be biased in the  $0.9 < z < 1.0$  bin due to the flux limit. We obtain 97.84% completeness in this bin for  $M_{F814W}$ , where completeness is defined as the ratio between the number of galaxies in  $m_{F814W} \leq 23.5$  and in  $m_{F814W} \leq 25.2$  samples. Thus the sample  $z \leq 1$  and  $M_{F814W} < -22$  is at least 97.84% complete. Figs. 2 & 3 show that at  $M_{F814W} < -22$ , we are not affected by flux limit yet.

The region between  $0.85 < z < 1.0$  is only moderately overdense and we do not seem to have as many underdense regions to compare with. It would rather be advantageous to disregard this region and redo the volume limiting procedure. We relax our luminosity cut so that the sample is volume-limited *not* until  $z = 1$  but until  $z = 0.85$ . We choose to impose the cut at  $M_{F814W} = -20.8$ , with 95.3% completeness in the  $0.8 < z \leq 0.85$  bin. This increases the sample size significantly, from 7,418 galaxies to 11,169. We call this sample S1.

However, previous studies **cite** have shown that absolute luminosities evolve with redshift. Thus, we must also let the luminosity cut evolve with the redshift. There has been no published literature on the LF for the  $I$ -band, particularly for the COSMOS survey. We used the published result (Faber et al. 2007) for the ‘rate’ of evolution of B-band magnitudes for DEEP2 and COMBO-17 surveys, which is  $\Delta M_B^* \sim -1.23$  mag per unit redshift, for both blue and red galaxies combined together. Typically, estimates of evolution in K-band are lesser than the estimates of evolution in B and V bands. Assuming that the evolution is a smooth function of the wavelength, the evolution in I-band is expected to be lesser than that of the B-band. Therefore, by considering no evolution and an upper bound on the evolution, we can interpolate what the results would be like for the true  $I$ -band evolution.

Thus, we construct a second volume-limited sample S2, this time by letting the luminosity cut evolve. Starting from  $M_{F814W} = -20.8$  for the  $0.8 < z \leq 0.85$  bin, we add to it 1.23 times the difference between the bincenters to obtain the luminosity cut for the other (lower) redshift bins. At



| Redshift   | Environment | S1   | S2   | S3   |
|------------|-------------|------|------|------|
| 0.3-0.4    | Overdense   | 1726 | 2505 | 1260 |
| 0.4-0.475  | Neutral     | 988  | 1317 | 710  |
| 0.475-0.55 | Neutral     | 1410 | 1788 | 902  |
| 0.55-0.65  | Underdense  | 1797 | 2193 | 1183 |
| 0.65-0.75  | Overdense   | 4059 | 4476 | 2593 |
| 0.75-0.8   | Underdense  | 1159 | 1196 | 675  |
| 0.8-0.85   | Overdense   | 2428 | 2428 | 1630 |

**Table 1.** List of different redshift bins, their environmental classification and the number of galaxies binwise for volume-limited samples constructed in three different ways: using hard luminosity cut (S1), letting the luminosity cut evolve with redshift (S2) and imposing stellar-mass cuts (S3).

lower redshifts, we allow for fainter galaxies that wouldn't have passed the cut in S1 and hence has more galaxies.

Alternatively, one could get around the problem of considering redshift evolution by imposing cuts on stellar mass instead of absolute luminosity in a particular band. In Fig. 4, we show the stellar mass function (SMF) of our sample for various F814W flux limit. Tomczak et al. (2014) report the SMFs for the ZFOURGE survey, which includes COSMOS. They considered for this work, a single stellar population following a Chabrier IMF (Chabrier 2003). We plot their SMF for *all* in Fig. 4 for reference. Their SMF is higher than ours since they reach  $K_s$ -band  $5\sigma$  depth of 24.9. As in the case of  $M_{F814W}$  s, we compare the stellar mass in the  $m_{F814W} \leq 23.5$  sample with that of the  $m_{F814W} \leq 25.2$  sample. The sample  $\log(M/M_\odot) > 10.15$  is about 95% complete in the redshift bin  $[0.75 - 0.85]$  and has 10,341 galaxies in total. Thus, we construct a third volume-limited sample S3 by imposing the stellar mass cut mentioned above. The number of galaxies in redshift slices are tabulated in Table 1 for all 3 ways of obtaining a volume-limited sample. Stellar-mass limited sample happens to be the smallest one.

There is a minor pitfall with this method. We analyse only those galaxies for which postage stamp images exist. 12% of galaxies that pass our cuts do not have an associated postage stamp image. Yet, we use the full  $m_{F814W} \leq 23.5$  sample, irrespective of the existence of postage stamps, for identifying overdensities and in the completeness calculation for volume-limiting. Postage stamps may not exist because, given the size of the galaxy, the size of the postage stamp we want to draw around it (including enough blank space) intersects with the edge of the CCD. If all galaxies were the same size, this would be a purely random effect, but in fact bigger galaxies are more likely to get excluded by this cut. Typically galaxies that are nearby and intrinsically very bright do not have postage stamps associated with them and this is an effect that is dominant at lower redshifts. Our completeness calculation is done at high redshifts and thus we believe that our conclusions are not affected by this bias.

The functional forms for the (flux-limited) redshift distribution that we used in §3.1 are not physically motivated. We fit them again to the redshift distribution of a volume-limited sample (S1). Referring to Fig. 5, the values of  $\delta_{g,1D}$  for the  $z = 0.40 - 0.55$  bin have increased and are within  $\pm 10\%$  of 0. This is the reason why in §3.1 we classified them as neutral as opposed to underdense. We will see in §4 that they are more similar to overdense regions as opposed to un-

derdense regions. The other redshift slices seem to exhibit a consistent behavior.

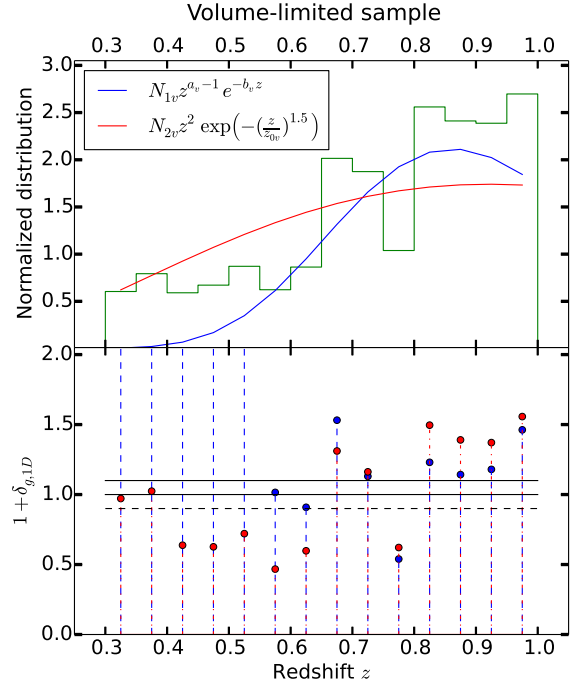


**Figure 5.** Upper panel: Redshift distribution of volume-limited ( $M_{F814W} < -20.8$ ) S1 sample with bins that are 0.05 wide. Two analytical functions with best fit parameters are plotted over it. Lower panel: Plot of  $(1 + \delta_{g,1D}) = N/N_{\text{mod}}$  with each functional form as the model for each redshift bin.

In the following section, we will compare and analyze the distribution of properties of the galaxies residing in the overdense regions.

### 3.3 Describing galaxy morphology and shape

In my opinion, given that the main results are from Claire's fits, you should describe those *first* and then put the re-Gaussianization description second. Also, state this plan up front, i.e., something like “To describe galaxy morphology and shape, we will use fits to Sérsic profiles. (... description here ...) However, as a secondary check on the results, we will use ...”

If galaxies have elliptical isophotes, its shape and size could be defined by the axis ratio and the area enclosed by a boundary isophote. However, in real galaxy images, the boundary may not be well defined and the shape may not be well approximated by an ellipse. More importantly, the effect of smearing due to the point-spread function (PSF) is larger. Thus, we are in need of more sophisticated methods to measure the ellipticities.

One method to estimate the ellipticities is to estimate the axis-ratios by fitting parametric models to each image. The models that we fit to the images are

- (i) a Sérsic profile given by the expression

$$S = \Sigma_{1/2} \exp \left( -k(R/R_{\text{eff}})^{1/n} - 1 \right), \quad (4)$$

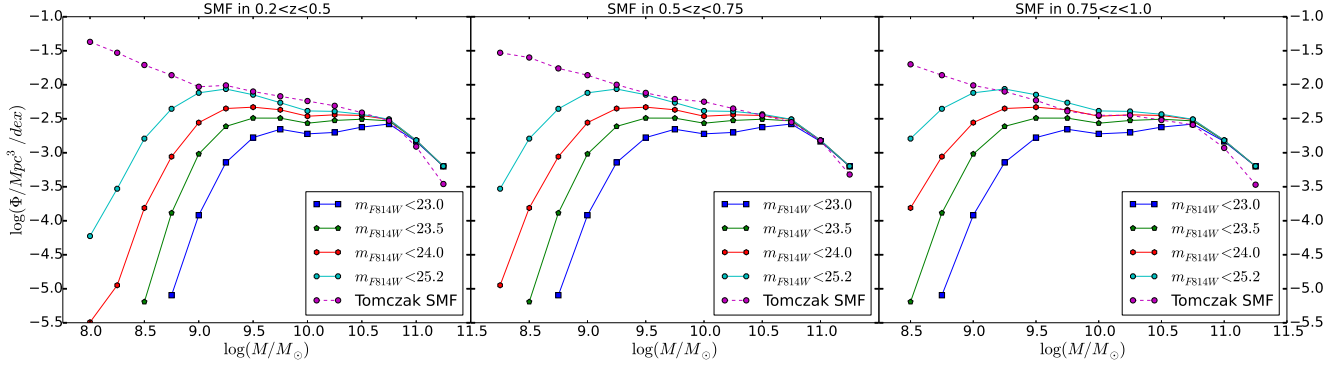


**Figure 4.** Stellar-mass distribution for various flux-limited samples in three redshift ranges are plotted. Bins have been chosen so as to make the comparison easier with a study of SMF in the same FOV (Tomczak et al. 2014). At high mass, the distributions are the same for various flux limits indicating that the samples are complete in that mass range. The curves begin to separate at low masses on account of incompleteness, which determines where the mass cutoff should be to volume-limit the sample.

(ii) two Sérsic component fits: de Vaucouleurs bulge ( $n = 4$ ) + exponential disc profile ( $n = 1$ ),

where

$$R^2 = ((x - x_0) \cos \Phi + (y - y_0) \sin \Phi)^2 + ((y - y_0) \cos \Phi - (x - x_0) \sin \Phi)^2 / q^2,$$

$R_{\text{eff}}$  is the half-light radius of the profile,  $\Sigma_{1/2}$  is the surface brightness at  $R = R_{\text{eff}}$ ,  $(x_0, y_0)$  is the centroid of the image,  $\Phi$  is the profile rotation angle,  $n$  is the Sérsic index,  $k$  is a  $n$ -dependent normalization factor and  $q$  is the axis ratio of the elliptical isophotes. Thus, the Sérsic profile has 7 free parameters. The bulge+disk model has 10 free parameters since the Sérsic indices are fixed as 1 and 4 and both the profiles are required to have the same centroid  $(x_0, y_0)$ . Best-fit parameters were found, by minimizing the weighted sum of the difference between the image and the PSF-convolved model using Levenberg-Marquardt minimization, `mpfit2fun` in IDL (Markwardt 2009). More details about the fit can be found in Lackner & Gunn (2012).

The quantities that we would use from the single Sérsic profile fits are the Sérsic index and axis ratio and from the bulge+disk fits will be the Bulge-to-Total ratio given by  $\Sigma_{1/2}(n=4)/(\Sigma_{1/2}(n=4) + \Sigma_{1/2}(n=1))$ .

An alternative method involves correcting the observed image for the PSF and computing the covariances from which the ellipticity of the galaxy can be obtained. The PSF correction scheme used on the observed images is that of ‘re-Gaussianization’ method described in §2.4 of Hirata & Seljak (2003) (hereafter HS03). This method models the true PSF  $g(\mathbf{x})$  as a Gaussian  $G(\mathbf{x})$  and the residual  $\epsilon(\mathbf{x}) = g(\mathbf{x}) - G(\mathbf{x})$  is assumed to be small. Thus, the Gaussian-convolved intrinsic image of  $f$ , is  $I' = G \otimes f = I - \epsilon \otimes f$ , where  $I$  is the observed image. The crucial idea here is that, when  $\epsilon$  is small, we get a reasonably accurate estimate of  $I'$  even if we use an approximate form for  $f$ . The form assumed for  $f$  is that of a Gaussian with covariance  $M_f^{(0)} = M_I - M_g$ , where  $M_I$  and  $M_g$  are the adaptive covariances of the measured object and PSF respectively, described in §2.1 of HS03, which is in turn based on Bernstein & Jarvis (2002). Once we obtain the covariance matrices of the intrinsic image  $f$ , one can compute

the ellipticities of the galaxies, which we will refer to as ‘ellipticities based on moments’.

## 4 RESULTS

Having identified the overdense and underdense regions in a volume-limited sample (§3.1, §3.2), we will now see in this section if the morphological parameters of the galaxies, listed in §3.3, have any dependence on the environment that they reside in. We have 3 different ways of volume-limiting our sample

- (i) no redshift evolution of luminosity cut (S1),
- (ii) use  $B$ -band evolution rate for  $I$ -band luminosities (S2),
- (iii) impose stellar mass cuts instead of luminosity (S3)

and we will present our results in each of the 3 cases. **Say how this connects to the 3 samples S1, S2, and S3 that you defined earlier. Done.**

**I also recommend splitting this section up into subsections so it's not just one big block. For example, the first can be about axis ratios (with a subsection about how the results depend on the way the volume limiting was carried out), the second can be about morphology from Sersic index and bulge-to-total ratios.**

### 4.1 Axis-ratios

We can understand the influence of environment on the ellipticities of the galaxies simply by comparing the distribution of the axis ratios for the overdense and underdense samples. Then, we proceed to consider the root mean square ellipticity, a statistic that can characterize the shape of the population/sample of galaxies.

#### 4.1.1 Comparing distributions

We use two statistical tests namely the Kolmogorov-Smirnov test and Anderson-Darling test to compare distributions.

We first compare the distribution of the axis ratio in *all* overdense bins and *all* underdense bins in Fig. 6. **How**

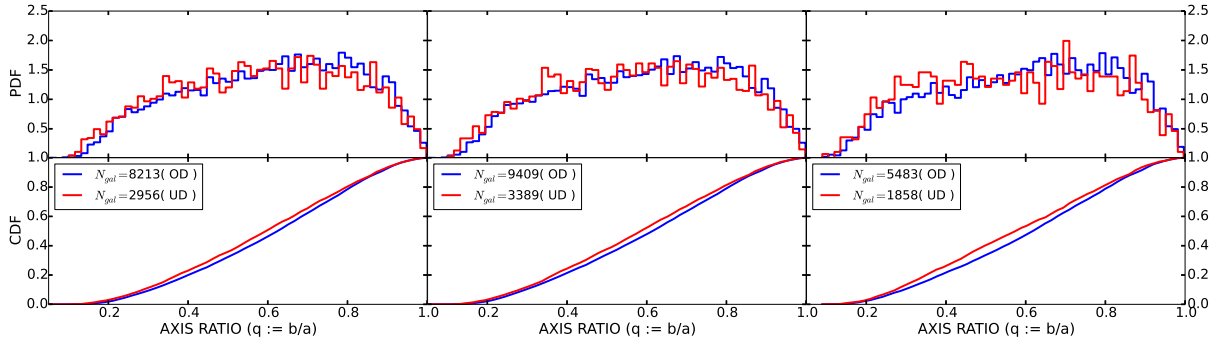


**Figure 6.** The distributions of axis ratios of galaxies in *all* overdense (OD) and *all* underdense (UD) regions in the case of luminosity-selected sample (left), luminosity-selected with B-band evolution taken into account (center) and stellar-mass-selected sample (right). The upper panels show the histogram and the bottom panels show the empirical cumulative distribution function (ECDF).  $p$ -values are computed using these CDFs using the Kolmogorov-Smirnov and Anderson-Darling tests and are given in Table. 2. The difference between the CDFs turn out to be statistically significant.

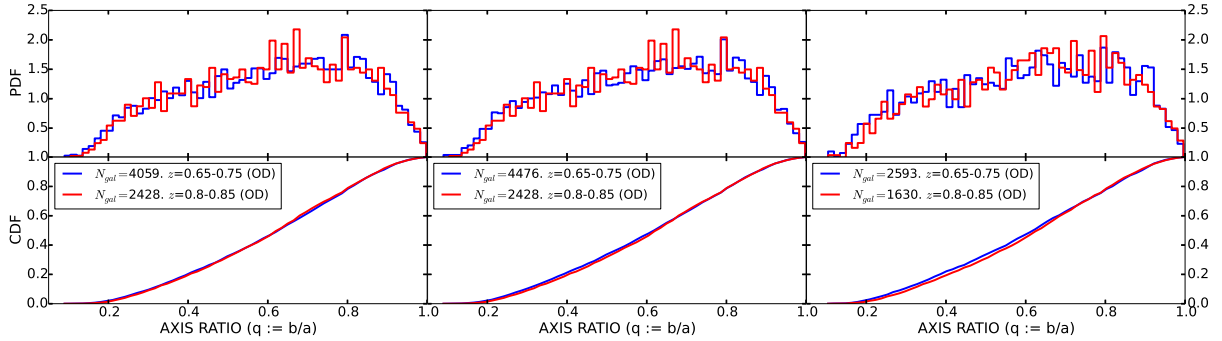


**Figure 7.** Comparison in similar environments: Axis ratios of galaxies in two overdense redshift bins,  $z = 0.65 - 0.75$  and  $z = 0.80 - 0.85$  are compared.  $p$ -values from the KS and AD test are given in Table. 2

| Redshift bins               | Tests | $S1$   | $S2$  | $S3$  |
|-----------------------------|-------|--------|-------|-------|
| All overdense vs.           | K-S   | 1.1e-4 | 3e-5  | 0.0   |
| All underdense              | A-D   | 1e-5   | 0.0   | 0.0   |
| $z : [0.65, 0.75]$ (OD) vs. | K-S   | 0.613  | 0.431 | 0.231 |
| $z : [0.80, 0.85]$ (OD)     | A-D   | 0.494  | 0.237 | 0.130 |
| $z : [0.65, 0.75]$ (OD) vs  | K-S   | 5.8e-4 | 2e-5  | 0.0   |
| $z : [0.55, 0.65]$ (UD)     | A-D   | 9.8e-4 | 0.0   | 0.0   |

**Table 2.**  $p$ -values from the Kolmogorov-Smirnov (K-S) and Anderson-Darling (A-D) obtained by comparing the distributions of axis ratios are given for three cases: *all* overdense (OD) vs. *all* underdense (UD), two overdense bins, not very separated in redshift and a pair of adjacent overdense and underdense bins.  $S1$ ,  $S2$ ,  $S3$  refer to the volume-limited sample in three different ways.

| Redshift bins               | Tests | $S1$    | $S2$    | $S3$    |
|-----------------------------|-------|---------|---------|---------|
| All overdense vs.           | K-S   | 0.00056 | 0.0001  | 0.0     |
| All underdense              | A-D   | 3e-5    | 1e-5    | 0.0     |
| $z : [0.65, 0.75]$ (OD) vs. | K-S   | 0.9563  | 0.7476  | 0.5359  |
| $z : [0.80, 0.85]$ (OD)     | A-D   | 0.5162  | 0.3352  | 0.2290  |
| $z : [0.65, 0.75]$ (OD) vs  | K-S   | 0.00605 | 0.00025 | 0.00024 |
| $z : [0.55, 0.65]$ (UD)     | A-D   | 0.01201 | 0.00025 | 5e-5    |

**Table 3.**  $p$ -values from the Kolmogorov-Smirnov (K-S) and Anderson-Darling (A-D) obtained by comparing the ellipticities computed using second moments are given for three cases: *all* overdense (OD) vs. *all* underdense (UD), two overdense bins, not very separated in redshift and a pair of adjacent overdense and underdense bins.  $S1$ ,  $S2$ ,  $S3$  refer to the volume-limited sample in three different ways.

was the volume-limiting carried out for this? You should say the answer to this question for all figures. Blue caption mentions it. Unless otherwise mentioned, the axis ratios refer to the values obtained using the method of Lackner & Gunn (2012). The cumulative distinction functions are also plotted alongside in order to be able to visualize the ‘distance’ between the distributions. Referring to the first two rows in Table 2, we see that the  $p$ -values from both the KS and AD

tests are well below 0.05 (give the actual numbers! It’s in the table. The text does not seem to mention the table at all. If readers are to get the numbers from it, then you need to refer to it here and any other place where it is relevant.), Done. so we reject the ‘null hypothesis’ that the overdense and underdense regions have same axis ratio distributions at 95% significance level.

One might imagine that the disagreement between the

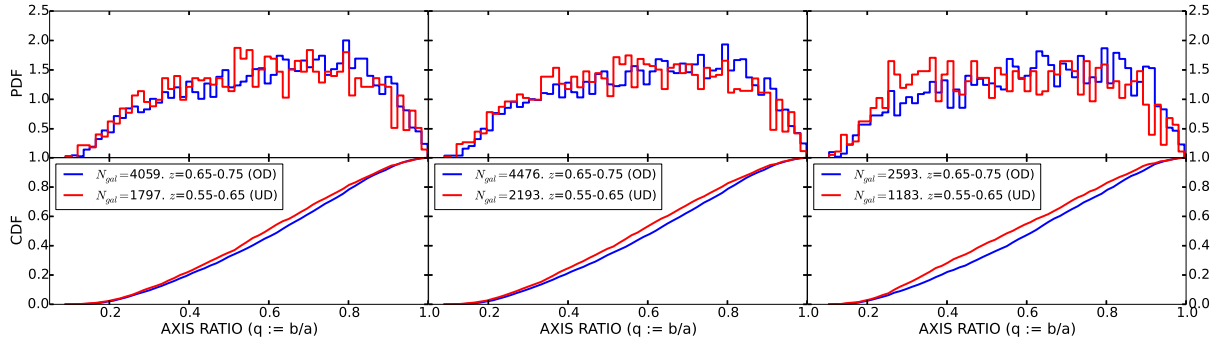


**Figure 8.** Comparison in contrasting environments: Axis ratios of galaxies in an underdense redshift bin,  $z = 0.55 - 0.65$  are compared with those in an overdense bin,  $z = 0.65 - 0.75$ .  $p$ -values from the KS and AD test are given in Table. 2

distributions is, at least partly, due to the fact that the overdense and underdense sample have different redshift distributions. To show that that is not the case, we will compare distributions between two overdense / underdense redshift bins, where we expect to find similarity, and between an overdense and underdense regions, where we expect the distributions to differ. Figures 7 and 8 are examples showing that the distributions are indeed similar when the environments are similar and different when the environments are different, confirming our expectation. Similar conclusion can be arrived at by comparing other redshift bins.

Such a trend is also observed in axis ratios based on second moments. I've commented on the agreement/disagreement of the distributions themselves in Table 3. No plots included. If  $Q_{ij}$  represents the generic matrix element of the matrix of second moments, then define a complex number, sometimes known as the *distortion*, as

$$e = e_1 + ie_2 = \frac{Q_{11} - Q_{22} + 2iQ_{12}}{Q_{11} + Q_{22}}. \quad (5)$$

Is this the correct denominator? Then, one definition of ellipticity is the magnitude of this complex number which is  $\sqrt{e_1^2 + e_2^2}$ .

After neglecting a small fraction ( $\sim 0.0065\%$ ) of galaxies (36 out of 55991 galaxies between  $0.3 \leq z < 0.85$  with  $\log(M/M_\odot) > 10.15$ ) for which the moments do not converge, we make comparisons to the above between the distribution of ellipticities computed from the second moments and the results are tabulated in Table 3. Once again, we see that the distributions are consistent with each other when the environment is similar and are inconsistent when the environments are contrasting.

#### 4.1.2 RMS ellipticities

For the luminosity-selected sample without any evolution, RMS ellipticities of galaxies in each redshift bin are shown in Figure 9. As one can see, the underdense regions have significantly higher values for RMS ellipticities when compared to the overdense regions. Note in particular that we've been able to capture the narrow overdense bin  $0.75 \leq z < 0.80$ . There is (almost) no redshift dependence in the figure.

The dependence on the local environment seems to make sense. Overdense regions typically have young, spiral galaxies which have high  $q$  and hence low RMS ellipticity.

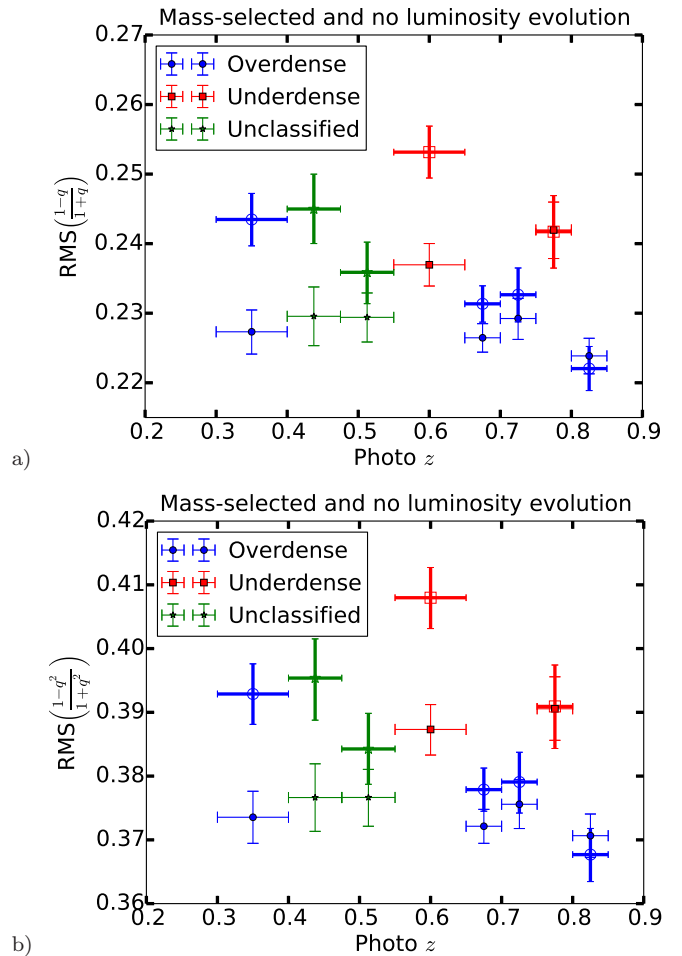


**Figure 9.** Left: RMS ellipticities with ellipticity defined as  $\frac{1-q}{1+q}$ . Right: RMS ellipticities with ellipticity defined as  $\frac{1-q^2}{1+q^2}$ . The horizontal errorbars simply correspond to the binwidth while the vertical ones are  $1\sigma$  errorbars obtained by bootstrapping.

On the contrary, the underdense regions typically have old, elliptical galaxies and thus low  $q$  and high RMS ellipticity.

From Figs. 1 and 5, the region  $0.4 \leq z < 0.55$  show signs of being marginally underdense but have low RMS



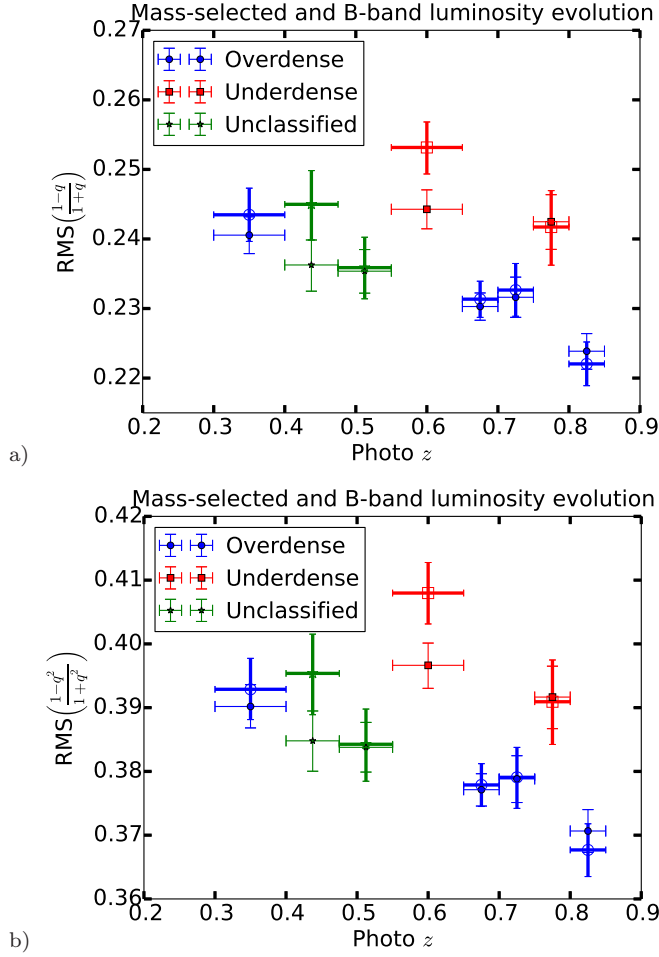


**Figure 10.** Left: RMS ellipticities with ellipticity defined as  $\frac{1-q}{1+q}$ . Right: RMS ellipticities with ellipticity defined as  $\frac{1-q^2}{1+q^2}$ . The horizontal errorbars simply correspond to the binwidth while the vertical ones are  $1\sigma$  errorbars obtained by bootstrapping. The solid points correspond to the sample where the luminosity cut evolves by  $-1.23$  per unit redshift (S2) and the unfilled points correspond to the sample obtained from stellar mass cuts (S3).

ellipticities too that agree with the rest of the overdense regions.

When the B-band luminosity evolution is taken into account in selecting the sample, a systematic increase in the ellipticity at lower redshifts can be observed. We plot these alongside with stellar-mass selected samples, where a similar trend is found, in Fig. 10. Also, the RMS values of the ellipticities calculated from the second moments within each redshift bin are given in Fig. 11.

#### 4.2 Other morphological parameters

For other morphological parameters such as the Sérsic index and Bulge-to-Total ratio, we do not compare the distributions themselves directly. For Sérsic profile fits, it gets tricky since we truncate the Sérsic index at 6. For Bulge-to-Total ratios, we force the value to be between 0.05 and 0.95. We will understand the dependence of these quantities

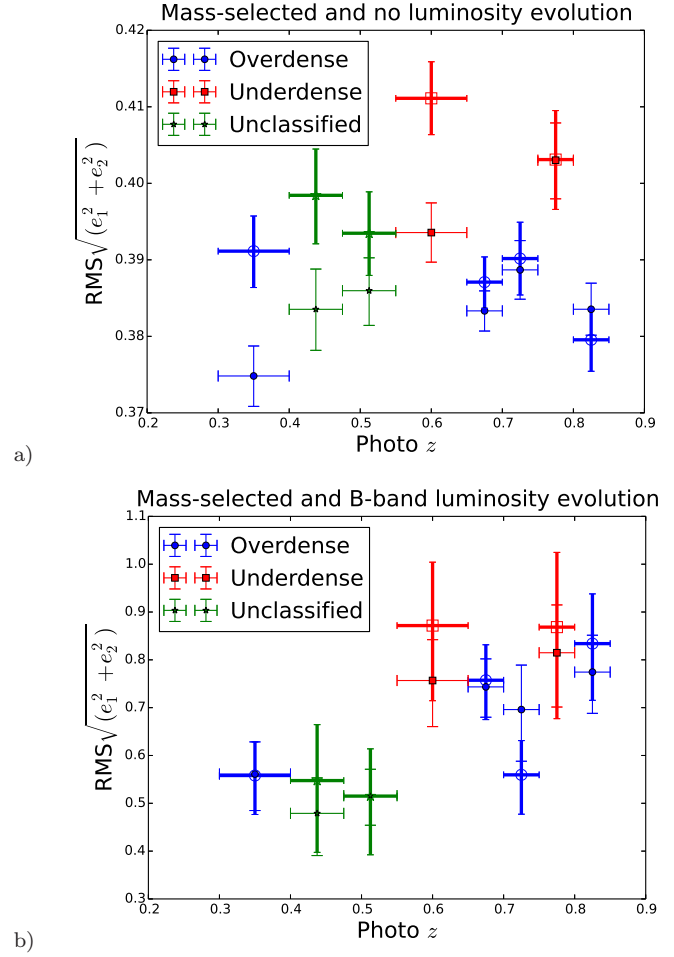


**Figure 11.** RMS ellipticities with ellipticity defined as  $\sqrt{e_1^2 + e_2^2}$ , where  $e_1$  and  $e_2$  are the real and imaginary components of the distortion defined in Eq. 5. The horizontal errorbars simply correspond to the binwidth while the vertical ones are  $1\sigma$  errorbars obtained by bootstrapping. The solid points correspond to the luminosity selected sample (S1 sample on the left and S2 sample on the right) and the unfilled points correspond to the sample obtained from stellar mass cuts (S3).

on environment by computing the median values in different redshift bins. We choose median over mean since it is more robust to the truncation effects. Fig. 12 show the median of the Sérsic index with and without taking into account of the luminosity evolution. Median values obtained using stellar mass selected samples are plotted alongside for reference. We observe that the overdense regions tend to have higher Sérsic index than the adjacent underdense ones. Fig. 13 show the variation of median Bulge-to-Total ratio with redshift. We see that the bulge component is more in overdense regions than in the underdense regions. These two observations are consistent with each other since higher Sérsic index implies higher bulge component which are typical in young galaxies found in overdense regions.

In Fig. 12, we see that the Sérsic indices of mass selected sample (S3) are systematically greater than those of the luminosity selected samples (S1,S2). This is consistent with the Bulge-to-Total values being higher in S3 than in

S1 or S2 in Fig. 13. This is not just an edge effect but can be seen from the distributions themselves that the mass selected sample doesn't include as many disk-like galaxies as in luminosity selected samples.

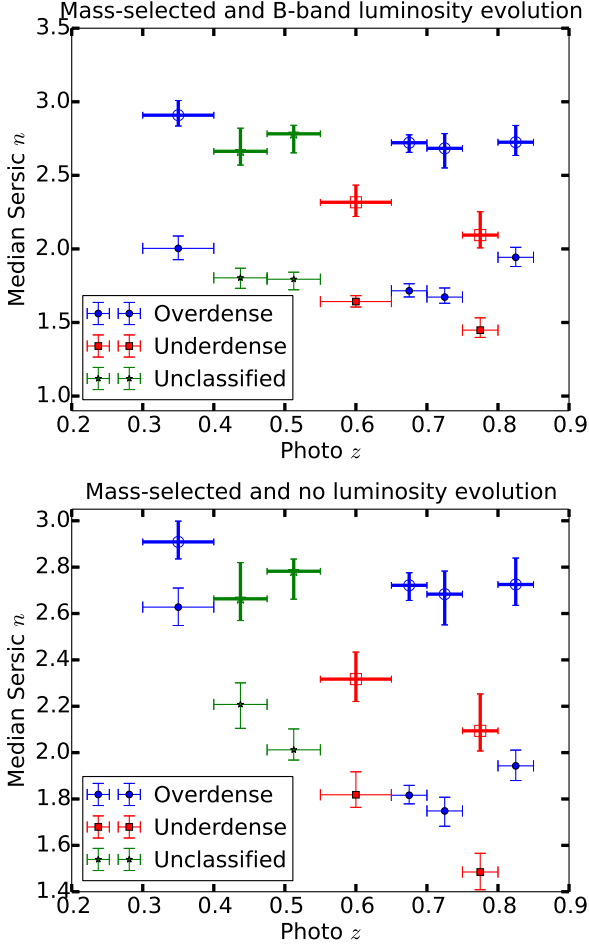


**Figure 12.** Median values of the Sérsic indices for volume-limited samples S1 and S3 are plotted (filled centers and thin errorbars) in left and right panels respectively for each redshift bin. Median values for the S2 sample are plotted in both the panels (open centers and thick errorbars) in both the panels. The horizontal errorbars simply correspond to the binwidth while the vertical ones are  $1\sigma$  errorbars obtained by bootstrapping.

## 5 CONCLUSIONS

In this study, we have shown that morphological parameters of galaxies depend on the local environments along the line of sight in a manner than affect Weak Lensing simulations. In studies of Weak Lensing, one simulates galaxy images in a redshift slice by learning from the images in the same redshift bin of a training sample like COSMOS, which we have used for our analysis here. The survey volume is broken up into multiple redshift slices and are classified as ‘overdense’, ‘underdense’ or ‘neutral’ according to their local environment. This is done by comparing the 1-D redshift distribution to some of the parametric models available in

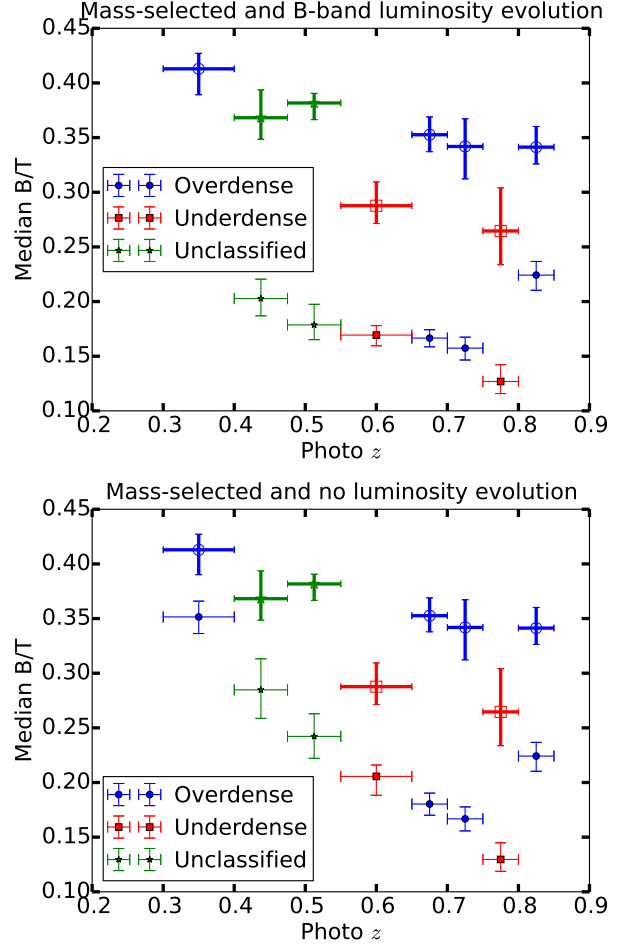


**Figure 13.** Median values of the Bulge-to-Total ratios for volume-limited samples S1 and S3 are plotted (filled centers and thin errorbars) in left and right panels respectively for each redshift bin. Median values for the S2 sample are plotted in both the panels (open centers and thick errorbars) in both the panels. The horizontal errorbars simply correspond to the binwidth while the vertical ones are  $1\sigma$  errorbars obtained by bootstrapping.

the literature. The incompleteness in the sample is minimized by constructing a volume limited sample either by imposing stellar mass cuts (S3) or by imposing a luminosity cut. Further, depending on whether we have the cut fixed or evolve with redshift, we get two more volume limited samples S1 and S2 respectively. Morphological parameters are obtained by fitting a single Sérsic profile to the images or by a two component (bulge+disk) fit. The morphological quantities of interest include axis ratios or equivalently the ellipticities, Sérsic indices and Bulge-to-Total ratios.

For all the three volume-limited samples, we compare the distributions of the axis-ratios of the galaxies in overdense and underdense regions and conclude that the distributions are different after performing statistical tests on them. From the axis ratios, we compute ellipticities and find that the root mean squared value of the ellipticities of galaxies in a redshift bin vary significantly between the overdense and underdense regions. Such a behavior is also observed when ellipticities are computed using second moments instead of a parametric model fitting. Sérsic index and Bulge-to-

Total ratios also exhibit similar trends with redshift based on the local environment.

Our result has serious implications for realistic image simulations for Weak Lensing. It suggests that the training sample is affected by cosmic variance so as to possibly bias the conclusions from the simulations. This is particularly a problem with narrow surveys where a single galaxy cluster or a void could affect the environment significantly. Thus, we are forced to use wider redshift bins, much larger than the uncertainties in the redshifts, so as to be able to wash out the environmental dependence. However, future surveys such as the Large Synoptic Survey Telescope (LSST; LSST Science Collaboration et al. 2009) will image larger areas of sky mitigating the dependence of local environment in image simulations.

## ACKNOWLEDGMENTS

AK and RM acknowledge the support of NASA ROSES 12-EUCLID12-0004, and program HST-AR-12857.01-A, provided by NASA through a grant from the Space Telescope Science Institute, which is operated by the Association of Universities for Research in Astronomy, Incorporated, under NASA contract NAS5-26555. RM acknowledges the support of an Alfred P. Sloan Research Fellowship. We thank Alexie Leauthaud for many useful discussions.

## REFERENCES

- Baugh C. M., Efstathiou G., 1993, *MNRAS*, 265, 145  
 Bernstein G. M., Jarvis M., 2002, *AJ*, 123, 583  
 Bundy K. et al., 2006, *ApJ*, 651, 120  
 Chabrier G., 2003, *PASP*, 115, 763  
 de Jong J. T. A. et al., 2013, *The Messenger*, 154, 44  
 Faber S. M. et al., 2007, *ApJ*, 665, 265  
 Green J. et al., 2012, *ArXiv e-prints*  
 Hirata C., Seljak U., 2003, *MNRAS*, 343, 459  
 Ilbert O. et al., 2009, *ApJ*, 690, 1236  
 Kaiser N. et al., 2010, in *Society of Photo-Optical Instrumentation Engineers (SPIE) Conference Series*, Vol. 7733, *Society of Photo-Optical Instrumentation Engineers (SPIE) Conference Series*  
 Koekemoer A. M. et al., 2007, *ApJS*, 172, 196  
 Kovač K. et al., 2010, *ApJ*, 708, 505  
 Lackner C. N., Gunn J. E., 2012, *MNRAS*, 421, 2277  
 Laureijs R. et al., 2011, *ArXiv e-prints*  
 Leauthaud A. et al., 2010, *ApJ*, 709, 97  
 Leauthaud A. et al., 2007, *ApJS*, 172, 219  
 LSST Science Collaboration et al., 2009, *ArXiv e-prints*  
 Mandelbaum R., Hirata C. M., Leauthaud A., Massey R. J., Rhodes J., 2011, *SHERA: SHEar Reconvolution Analysis*. *Astrophysics Source Code Library*  
 Mandelbaum R. et al., 2014, *ApJS*, 212, 5  
 Markwardt C. B., 2009, in *Astronomical Society of the Pacific Conference Series*, Vol. 411, *Astronomical Data Analysis Software and Systems XVIII*, Bohlender D. A., Durand D., Dowler P., eds., p. 251  
 Miyazaki S. et al., 2006, in *Society of Photo-Optical Instrumentation Engineers (SPIE) Conference Series*, Vol. 6269, *Society of Photo-Optical Instrumentation Engineers (SPIE) Conference Series*  
 Scoville N. et al., 2007, *ApJS*, 172, 1  
 The Dark Energy Survey Collaboration, 2005, *ArXiv Astrophysics e-prints*  
 Tomczak A. R. et al., 2014, *ApJ*, 783, 85